

Spontaneous Phase Balancing in Delta-Connected Single-Phase Droop-Controlled Inverters

Minghui Lu , Member, IEEE, Sairaj Dhople , Member, IEEE, Donny Zimmanck, and Brian Johnson , Member, IEEE

Abstract—Power grids are evolving toward a highly distributed architecture with power-electronics circuits interfacing a majority of generation, storage, and loads. To ensure stability as synchronous machines are retired, grid-forming (GFM) inverters will be needed across the board. In this article, we investigate whether systems built with interconnected single-phase droop-controlled GFM inverters are capable of self organizing into balanced three-phase systems. We model, analyze, and build a system comprised of three delta-connected droop-controlled single-phase inverters connected across loads. After deriving a model of the angle dynamics for this system, we show that its stable equilibria coincide with balanced conditions, where each phase is offset by $1/3$ of an ac cycle. Furthermore, we observe that the desirable equilibrium with balanced phase offsets is robust against voltage and load imbalances. This demonstrates the feasibility of assembling three-phase systems using fleets of decentralized single-phase GFM inverters. The analytical developments are substantiated experimentally on a system of three delta-connected single-phase inverters. Spontaneous emergence of phase balancing from startup with nonidentical initial conditions are validated in the experimental setup. Empirical observations further illustrate robust operation during unbalanced conditions.

Index Terms—Delta connection, droop control, grid-forming (GFM) inverters, phase balancing.

I. INTRODUCTION

THIS article forges a path of possibilities where fleets of single-phase grid-forming (GFM) inverters can be used to create large grids. As power electronics are more deeply interwoven into grids and machines recede into a supportive role, it is paramount to ensure that ac phases in three-phase systems are offset by $2\pi/3$ rad (i.e., $1/3$ of an ac cycle). Windings on synchronous generators are spatially arranged to offer $2\pi/3$ rad phase separation in electrical outputs by design.

Manuscript received 11 May 2022; accepted 22 June 2022. Date of publication 27 June 2022; date of current version 6 September 2022. This work was supported by the U.S. Department of Energy's Office of Energy Efficiency and Renewable Energy (EERE) under Solar Energy Technologies Office (SETO) Agreement EE0009025. Recommended for publication by Associate Editor Y. Xue. (Corresponding author: Minghui Lu.)

Minghui Lu and Brian Johnson are with the Department of Electrical and Computer Engineering, University of Texas Austin, Austin, TX 78712 USA (e-mail: mhl@u.texas.edu; b.johnson@utexas.edu).

Sairaj Dhople is with the Department of Electrical and Computer Engineering, University of Minnesota Twin Cities, Minneapolis, MN 55455 USA (e-mail: sdhople@umn.edu).

Donny Zimmanck is with the Enphase Energy Inc, Fremont, CA 47281 USA (e-mail: dzimmanck@enphaseenergy.com).

Color versions of one or more figures in this article are available at <https://doi.org/10.1109/TPEL.2022.3186337>.

Digital Object Identifier 10.1109/TPEL.2022.3186337

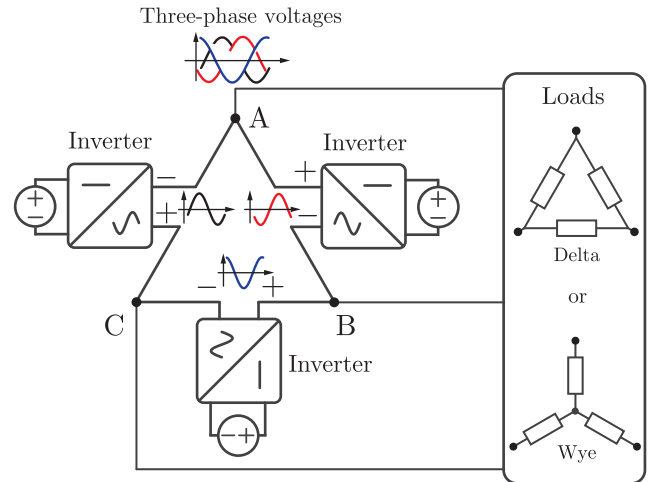


Fig. 1. Delta-connected single-phase droop-controlled GFM inverters delivering power to loads. We show that such a system is able to spontaneously reach phase-balanced operation with $2\pi/3$ rad phase offsets between inverter output voltages with no external communication.

Similarly, controllers for three-phase inverters enforce $2\pi/3$ rad phase angular offsets between waveforms on output terminals. Now, consider the case where large numbers of single-phase inverters with GFM controls are dispersed across a grid. Such a scenario is likely to be commonplace in future grids with power-electronics circuits taking center stage in energy conversion across single- and three-phase grids. Envisioning such a future scenario, we ponder over the following question in this article: can single-phase GFM inverters maintain requisite $2\pi/3$ rad offsets between phases in the absence of three-phase machines and three-phase inverters elsewhere? We conclusively show that delta-connected droop-controlled single-phase inverters exhibit repulsive coupling between phases such that balanced three-phase voltage waveforms can be generated in the system. We also provide a counterexample which illustrates the inability of wye-connected inverters to offer this capability. Hence, while GFM single-phase controllers carry out their intended purpose of voltage and frequency regulation, they also offer the bonus feature of balanced three-phase voltages when interconnected in a delta configuration. This demonstrates that fleets of decentralized single-phase droop-controlled inverters can power three-phase loads and provide a foundation to realize larger three-phase grids. (See Fig. 1.) Furthermore, the work establishes the possibility of single-phase GFM inverters being

able to support three-phase loads in settings where distribution networks are isolated or operated as a microgrid. Such an approach could significantly improve the resiliency and availability of distribution networks.

The application area we examine, i.e., GFM inverters, is of significant contemporary interest to the power industry at large, further establishing the need for in-depth investigations into a full range of capabilities of these technologies [1], [2]. Despite the growing body of work on GFM controls, to the best of our knowledge, there are no published works focused on the feasibility of using interconnected single-phase inverters as the foundation in three-phase systems. The majority of existing research on multiinverter systems is focused on three- (or single-) phase systems built exclusively with three- (or single-) phase inverters. The exception is the handful of results in [3] and [4], where single-phase inverters hang off a three-phase system that is propped up by three-phase inverters. In such a mixed system, the three-phase units are typically equipped with GFM controls to ensure system-wide frequency regulation.

Another line of existing work that should be acknowledged is that on coupled oscillator systems. In a context relevant here, parallel-connected inverters with GFM functions, such as droop and virtual oscillator control, can be modeled as coupled oscillators [5]–[7]. Many papers have uncovered why such systems synchronize their waveforms with theoretical methods inspired from literature pertaining to the dynamics of nonlinear oscillators. On the flip side, coupled oscillator theory has also been used to inspire methods for obtaining repulsive angular dynamics where oscillators converge to a steady state with angular offsets between them. In essence, this is the opposite of synchronization and the configuration where N oscillators are uniformly $2\pi/N$ apart is called the *splay* condition [8]–[11]. With regard to power applications, such notions are relevant to engineer decentralized controllers that yield interleaved pulsewidth modulation (PWM) carriers between converters [11]–[14] for purposes of ripple cancellation. Of particular relevance to this article, it is also known that a simple sign-flip in the feedback path of particular oscillators changes whether a system of coupled oscillators reaches phase-synchronized or -balanced (which includes $2\pi/N$ offsets) trajectories [5], [15].

To establish an analytical foundation and streamline analysis, we focus on the simplest case of three identical delta-connected droop-controlled single-phase inverters, as shown in Fig. 1, and reserve a more complete analysis for complex networks for future work. Our focus on the delta connection is deliberate since it is what gives the physical coupling between phases. In practical distribution systems with large numbers of single-phase GFM units, the delta-connected side of a substation transformer would provide the requisite interconnection to facilitate repulsive coupling between phases. After we define the nonlinear dynamical system, we compute its equilibria along with its linearized counterpart. We conclusively show that, out of all possible equilibria, it is only the phase-balanced condition with $2\pi/3$ rad offsets that is small-signal stable. In summary, our analytical findings, i.e., obtaining phase-balanced operation with delta-connected single-phase grid-forming inverters in a decentralized and communication-free manner, provide

significant contributions to the literature on power converter control, nonlinear dynamics, and coupled-oscillator systems, underscoring the motivation and significance of this work. This article is rounded off with experiments that showcase high performance over a spectrum of conditions. We also consider realistic load and generation imbalances that can be anticipated in practice and empirically show robust behavior in both experiments and simulations.

The rest of this article is organized as follows: In Section II, we introduce the delta-connected single-phase inverter setup along with the droop controllers utilized for GFM operation. Section III presents the dynamical-system model for the system. We then compute the angle equilibria and evaluate small-signal stability via a small-signal model in Section IV. Section V outlines the experimental results to validate the concept. Finally, Section VI concludes this article.

II. DELTA-CONNECTED INVERTERS AND DROOP CONTROL FOR GFM OPERATION

In this section, we introduce the delta-connected single-phase inverter system and the corresponding inverter controllers. We also introduce relevant notation along the way.

A. System Architecture

Fig. 1 shows a system of three single-phase inverters connected in a delta configuration on their ac sides. The negative terminal of each inverter connects to the positive terminal of the adjacent inverter when moving clockwise around the diagram loop. These inverters operate independently of each other without any communication beyond their intrinsic physical coupling. Three-phase loads can be connected in either wye or delta across the inverter system. While our analysis examines balanced loads, we consider both balanced and unbalanced load conditions in subsequent sections that include experimental validation. Each inverter has independent control loops that modulate its respective power stage.

B. Inverter Description

To facilitate multiinverter system analysis, we introduce the subscript index $\ell \in \{1, 2, 3\}$ to denote the three units in the system. The power stage and controller for the ℓ th inverter are illustrated in Fig. 2. The ac output produced by the H-bridge is fed to an *LCL* filter. The grid-side branch of each filter has resistance R , inductance L , and its inductive reactance is denoted by $X = \omega_{\text{nom}}L$, where ω_{nom} is the nominal system frequency. Examining the ℓ th *LCL* filter, the grid-side branch carries current i_ℓ and its midpoint capacitance is C_f with voltage v_ℓ across it. The inverter-side inductance is denoted by L_f . As illustrated at the top of Fig. 2, the phasor voltage across the ℓ th *LCL*-filter capacitive branch is denoted by

$$\bar{V}_\ell = V_\ell \angle \theta_\ell \quad (1)$$

where V_ℓ is the voltage rms magnitude and θ_ℓ is the time integral of ω_ℓ . Similarly, \bar{I}_ℓ is the phasor for the output current which flows through the complex impedance $\bar{Z} = R + jX$. Next, we

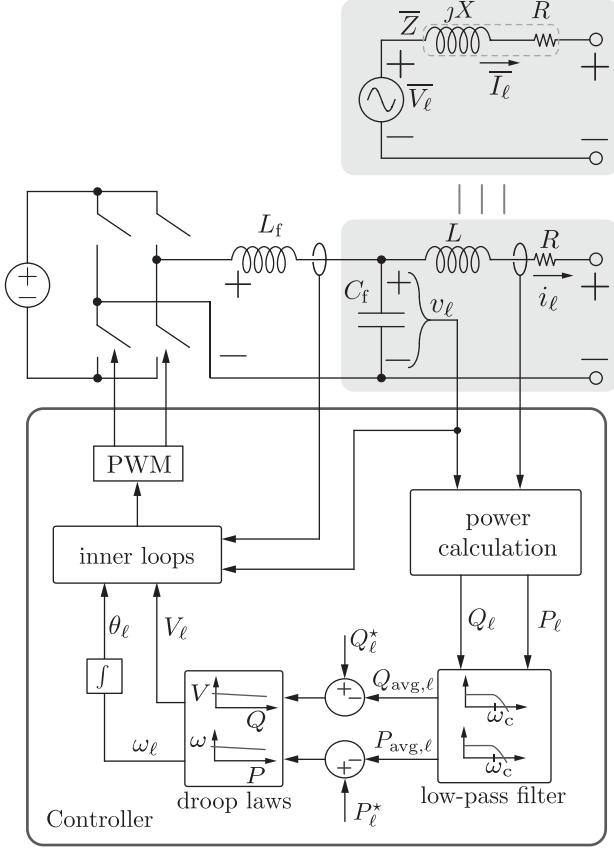


Fig. 2. (Bottom) Up-close look at the ℓ th inverter with droop control. Measurements from the LCL filter output are processed by the droop laws which, in turn, feed inner loops that regulate the capacitor voltage. (Top) Phasor-domain model that captures output terminal behavior. This model neglects the ultrafast dynamics of the inner loops and assumes the droop commands are ideally enforced for the voltage across the filter capacitor.

outline how droop laws govern the voltage magnitude V_ℓ and frequency ω_ℓ . With regard to notation, the voltage phasor will be interchangeably expressed in the forms $\bar{V}_\ell = V_\ell(\cos \theta_\ell + j \sin \theta_\ell) = V_\ell e^{j\theta_\ell}$, where $j^2 = -1$.

The ℓ th single-phase inverter has a droop controller that generates a reference-voltage waveform with amplitude V_ℓ and angle θ_ℓ such that the instantaneous sinusoidal command is $v_\ell^* = \sqrt{2}V_\ell \cos \theta_\ell$. The orthogonal version of the voltage command is denoted by $v_\ell^{\perp*} = \sqrt{2}V_\ell \cos(\theta_\ell - \pi/2)$. Inner control loops ensure that the voltage v_ℓ closely tracks the droop-generated voltage reference v_ℓ^* . Since these inner loops are much faster than the slow-acting droop dynamics, we will neglect them from here forward and assume that $v_\ell = v_\ell^*$. This is to facilitate analytical developments; rigorous analysis based on, e.g., singular-perturbation can be leveraged to justify the elimination of such dynamics (see, e.g., [7]).

The commanded amplitude and frequency for the ℓ th inverter are given by the droop laws

$$V_\ell = V_{\text{nom}} - m_q (Q_{\text{avg},\ell} - Q_\ell^*) \quad (2a)$$

$$\omega_\ell = \omega_{\text{nom}} - m_p (P_{\text{avg},\ell} - P_\ell^*). \quad (2b)$$

TABLE I
EXPERIMENTAL HARDWARE AND CONTROL PARAMETERS

Symbol	Description	Value	Units
S_{rated}	Inverter power	500	W
V_{nom}	Nominal voltage	80	V (rms)
ω_{nom}	Nominal frequency	$2\pi 60$	rad/s
f_{sw}	Switching frequency	20	kHz
L_f	Filter inductance	3	mH
C_f	Filter capacitance	20	μF
L	Filter inductance	0.94	mH
R	Filter resistance	0.28	Ω
$ \bar{Z}_{\text{loop}} $	Impedance magnitude	1.35	Ω
K	Constant in (14)	29.87	V
$\Delta\omega_{\text{max}}$	Frequency deviation	$2\pi 0.5$	rad/s
ΔV_{max}	Voltage deviation	$0.05 V_{\text{nom}}$	V
m_p	Droop slope	6.3×10^{-3}	V/W
m_q	Droop slope	8.0×10^{-3}	rad/(sVar)
ω_c	LP filter bandwidth	$2\pi 10$	rad/s

Above, V_{nom} and ω_{nom} are the nominal voltage amplitude and frequency, respectively. These are assumed to be equal for all three inverters. Furthermore, $P_{\text{avg},\ell}$ and $Q_{\text{avg},\ell}$ are filtered active- and reactive-power measurements, respectively; the corresponding setpoints are denoted by P_ℓ^* and Q_ℓ^* [16], [17]. The values of P_ℓ^* and Q_ℓ^* can be internally generated or be received by an exogenous secondary-control layer. For the purposes of this study, we will assume they are fixed. The droop slopes, m_q and m_p , are selected to give a 5% voltage deviation and 0.5-Hz frequency swing, respectively, as the apparent power varies across S_{rated} . This can be achieved with the choices

$$m_q = 0.05 \frac{V_{\text{nom}}}{S_{\text{rated}}}, \quad m_p = \frac{2\pi \times 0.5}{S_{\text{rated}}}.$$

The filtered active- and reactive-power values, $P_{\text{avg},\ell}$ and $Q_{\text{avg},\ell}$, are obtained via first-order low-pass filters with dynamics

$$\dot{P}_{\text{avg},\ell} = \omega_c (P_\ell - P_{\text{avg},\ell}) \quad (3a)$$

$$\dot{Q}_{\text{avg},\ell} = \omega_c (Q_\ell - Q_{\text{avg},\ell}), \quad (3b)$$

where $P_\ell = v_\ell i_\ell$ and $Q_\ell = v_\ell^\perp i_\ell$, denote the instantaneous active- and reactive-power values. The cutoff frequency ω_c should be sufficiently small to eliminate double-frequency pulsations in P_ℓ and Q_ℓ ; typical values of ω_c range from several Hz to tens of Hz.

C. Motivating Example

We provide simulation results for a system of three identical droop-controlled single-phase inverters connected in either wye or delta configurations to illustrate the phenomena we wish to examine in detail. In both configurations, the inverters are connected across a balanced wye-connected load. See Fig. 3 for an illustration of the simulation setup. Relevant parameters for the inverters are listed in Table I. Consider the configuration in Fig. 3(a), where the inverters are connected in wye. As the corresponding waveforms show, the inverters operate undisturbed

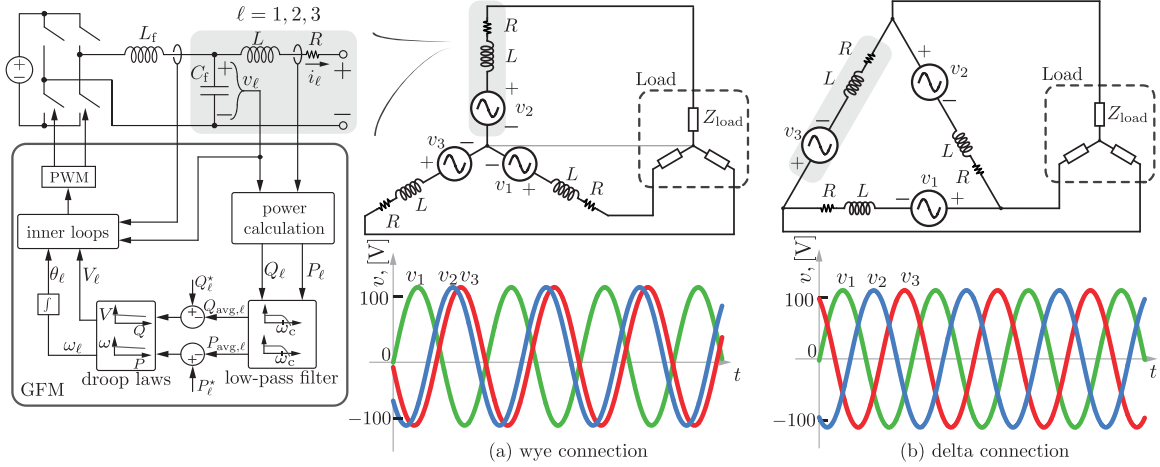


Fig. 3. Simulation setup involving interconnection of single-phase GFM inverters in (a) wye, and (b) delta configuration across a balanced wye-connected load. For the delta-interconnection of inverters, we readily obtain phase-balanced voltages, while the wye-interconnection does not yield such behavior naturally.

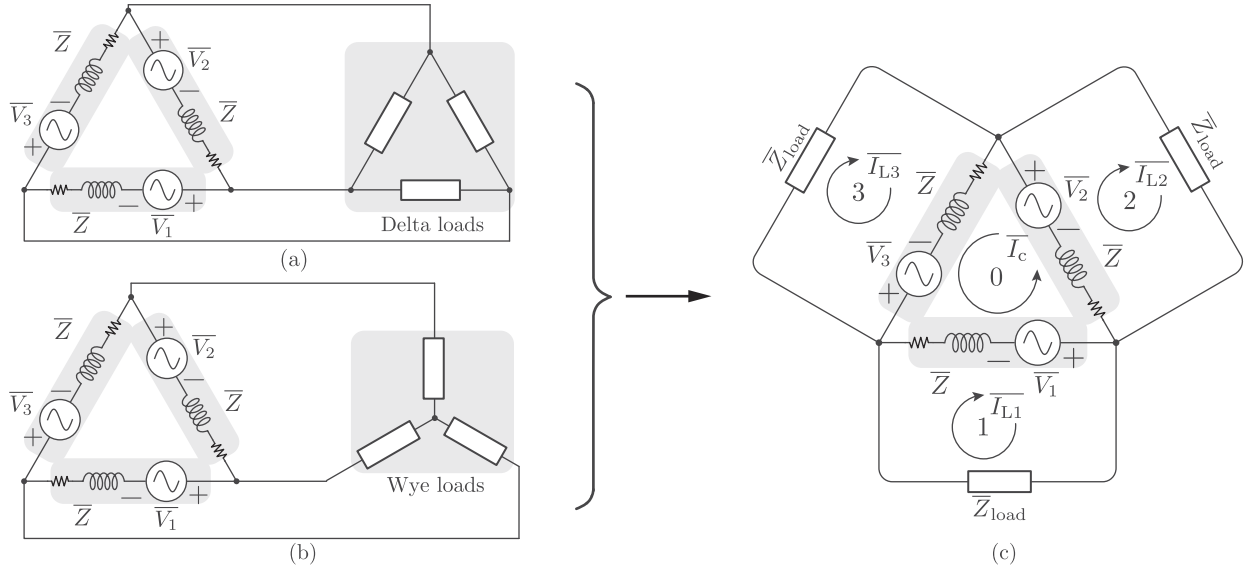


Fig. 4. Phasor representation of delta-connected inverters with: (a) delta loads, (b) wye loads, and (c) the equivalent diagram marking mesh-current phasors.

with phase offsets not equal to $2\pi/3$ indefinitely. (We remark that this imbalance persists even with a delta-connected load.) Next, we turn our attention to the setup in Fig. 3(b) which aligns with the focus of the article. Here, the inverters are delta-connected across the same load. The corresponding voltage waveforms are phase balanced in this setup. Reflecting on this simulation exercise, we note that the only difference between the systems in Fig. 3(a) and (b) is the physical interconnection of the inverters. In the subsequent sections, we will show that the droop controllers and circuit physics offered by the delta connection act to stabilize voltages around the phase-balanced operating point.

III. SYSTEM MODELING AND DYNAMICS

We now define additional phasor-domain quantities of interest and formulate a dynamical model for the delta-connected inverters. Ultimately, the following analysis will reveal that the

power circulating within the delta loop provides coupling and ensures angle dynamics settle to a phase-balanced equilibrium condition.

A. Inverter Active and Reactive Powers

With the single inverter phasor model on the top of Fig. 2, the delta-connected system takes the form in Fig. 4. In particular, each branch within the delta configuration captures the output terminal behavior of a droop-controlled inverter. Loads in delta and wye configurations are shown in Fig. 4(a) and (b), respectively. The delta-to-wye transformation allows us to cast both load configurations equivalently as the load in Fig. 3(c) [18]. Forthcoming analysis is therefore, tailored to the circuit representation in Fig. 4(c).

We apply Kirchhoff's laws following the *mesh current method* [19] that breaks the circuit system in Fig. 4(c) into

multiple loops. The current phasor in each loop is first computed independently, and then added together appropriately to recover branch currents. Along those lines, \overline{I}_c denotes the current phasor circulating within the inverter delta loop [this is the counterclockwise loop labeled #0 in Fig. 4(c)] while currents that flow through mesh loops #1, #2, and #3 are denoted by \overline{I}_{L1} , \overline{I}_{L2} , and \overline{I}_{L3} , respectively. Application of the superposition principle allows us to add \overline{I}_c and $\overline{I}_{L\ell}$ to obtain the branch currents corresponding to the ℓ th inverter, \overline{I}_ℓ . In particular, we can write

$$\overline{I}_\ell = \overline{I}_c + \overline{I}_{L\ell}. \quad (4)$$

We will see that mesh currents capture all phenomena of interest. In particular, \overline{I}_c reflects the loop coupling among three delta-connected inverters, while \overline{I}_{L1} , \overline{I}_{L2} , and \overline{I}_{L3} capture load effects. Application of Kirchhoff's voltage law yields

$$\overline{I}_c = \frac{1}{\overline{Z}_{\text{loop}}} \sum_{k=1}^3 \overline{V}_k \quad (5)$$

where

$$\overline{Z}_{\text{loop}} = R_{\text{loop}} + jX_{\text{loop}} = 3(R + jX)$$

is the total impedance around the delta loop. In addition, the expression for $\overline{I}_{L\ell}$ is given by

$$\overline{I}_{L\ell} = \frac{\overline{V}_\ell}{\overline{Z}_{\text{load}} + \overline{Z}} \quad (6)$$

where $\overline{Z}_{\text{load}} = R_{\text{load}} + jX_{\text{load}}$ is the load impedance and $\overline{Z} = R + jX$ is the inverter filter impedance. (Note that the load impedance $\overline{Z}_{\text{load}}$ is typically much larger than the filter impedance \overline{Z} .)

To reflect the droop dynamics in the circuit laws, we first calculate the apparent power \overline{S}_ℓ delivered by each inverter. This can be expressed as

$$\overline{S}_\ell = \overline{V}_\ell \overline{I}_\ell^* = \overline{V}_\ell \overline{I}_c^* + \overline{V}_\ell \overline{I}_{L\ell}^* \quad (7)$$

where $(\cdot)^*$ denotes the complex conjugate. We can show that the first term in the expression above for the apparent power, $\overline{V}_\ell \overline{I}_c^*$, can be expressed as

$$\overline{V}_\ell \overline{I}_c^* = \sum_{k=1}^3 \frac{V_k V_\ell}{|\overline{Z}_{\text{loop}}|} (\cos(\theta_{k\ell} - \phi) - j \sin(\theta_{k\ell} - \phi)) \quad (8)$$

where $\theta_{k\ell} = \theta_k - \theta_\ell$, $|\overline{Z}_{\text{loop}}|$ and ϕ denote the magnitude and angle of the delta-loop impedance, respectively, and are given by

$$|\overline{Z}_{\text{loop}}| = \sqrt{R_{\text{loop}}^2 + X_{\text{loop}}^2}, \quad \phi = \tan^{-1} \left(\frac{X_{\text{loop}}}{R_{\text{loop}}} \right).$$

Similarly, recognizing that the apparent power consumed by the load, $\overline{Z}_{\text{load}}$, dominates over that corresponding to the inverter

output filter, \overline{Z} , we can approximate the second term, $\overline{V}_\ell \overline{I}_{L\ell}^*$, simply as the apparent load power. In particular,

$$\overline{V}_\ell \overline{I}_{L\ell}^* \approx P_{\text{load}} + jQ_{\text{load}}. \quad (9)$$

Note that the approximation above is predicated on the assumption that the apparent power consumed by the output filter is negligible and holds more tightly for heavier loads. From (8) and (9), we can tease out the active- and reactive-power components of \overline{S}_ℓ , as

$$P_\ell \approx \sum_{k=1}^3 \frac{V_k V_\ell \cos(\theta_{k\ell} - \phi)}{|\overline{Z}_{\text{loop}}|} + P_{\text{load}} \quad (10a)$$

$$Q_\ell \approx - \sum_{k=1}^3 \frac{V_k V_\ell \sin(\theta_{k\ell} - \phi)}{|\overline{Z}_{\text{loop}}|} + Q_{\text{load}}. \quad (10b)$$

Next, we integrate the active- and reactive-power expressions from above explicitly with the droop laws for the inverters to obtain a dynamical model for the equation shown at the bottom of this page.

B. System Dynamical Equations

To derive the dynamical model for the phase dynamics of the GFM inverters, we will make a couple of simplifying assumptions. First, we will disregard the dynamics of the low-pass averaging filters in (3) and suppose that $P_{\text{avg},\ell} \approx P_\ell$ and $Q_{\text{avg},\ell} \approx Q_\ell$. We will also suppose that nominal power setpoints are fixed at $P_\ell^* = P_{\text{load}}$ and $Q_\ell^* = Q_{\text{load}}$. This is a reasonable assumption, since power setpoints are anticipated to match the nominal load (and/or updated via secondary control to match real-time load). Substituting P_ℓ , Q_ℓ from (10) directly in (2) and setting $P_\ell^* = P_{\text{load}}$, $Q_\ell^* = Q_{\text{load}}$, we get

$$V_\ell = V_{\text{nom}} + m_q \sum_{k=1}^3 \frac{V_k V_\ell}{|\overline{Z}_{\text{loop}}|} \sin(\theta_{k\ell} - \phi) \quad (12a)$$

$$\dot{\theta}_\ell = \omega_{\text{nom}} - m_p \sum_{k=1}^3 \frac{V_k V_\ell}{|\overline{Z}_{\text{loop}}|} \cos(\theta_{k\ell} - \phi). \quad (12b)$$

Note that the above model couples phase-angle dynamics with the voltage-droop laws. To simplify analysis, we combine the two, and with appropriate assumptions, generate a dynamical model for phase differences that is amenable to analysis.

IV. PHASE-BALANCING BEHAVIOR AND STABILITY

In this section, we establish the dynamics of the phase-angle differences and identify their equilibria. We then examine the small-signal stability of each equilibrium point. To capture a spectrum of possible output impedances, we generalize our analysis with respect to the output impedance angle ϕ .

$$\mathcal{J}(\theta_{21,\text{eq}}, \theta_{31,\text{eq}}) = K \begin{bmatrix} (2 \cos \theta_{21,\text{eq}} + \cos(\theta_{21,\text{eq}} - \theta_{31,\text{eq}})) \sin \phi & (\cos \theta_{31,\text{eq}} - \cos(\theta_{21,\text{eq}} - \theta_{31,\text{eq}})) \sin \phi \\ + \sin(\theta_{21,\text{eq}} - \theta_{31,\text{eq}}) \cos \phi & + (\sin(\theta_{31,\text{eq}} - \theta_{21,\text{eq}}) - \sin \theta_{31,\text{eq}}) \cos \phi \\ \hline (\cos \theta_{21,\text{eq}} - \cos(\theta_{31,\text{eq}} - \theta_{21,\text{eq}})) \sin \phi & (2 \cos \theta_{31,\text{eq}} + \cos(\theta_{31,\text{eq}} - \theta_{21,\text{eq}})) \sin \phi \\ + (\sin(\theta_{21,\text{eq}} - \theta_{31,\text{eq}}) - \sin \theta_{21,\text{eq}}) \cos \phi & + \sin(\theta_{31,\text{eq}} - \theta_{21,\text{eq}}) \cos \phi \end{bmatrix}. \quad (11)$$

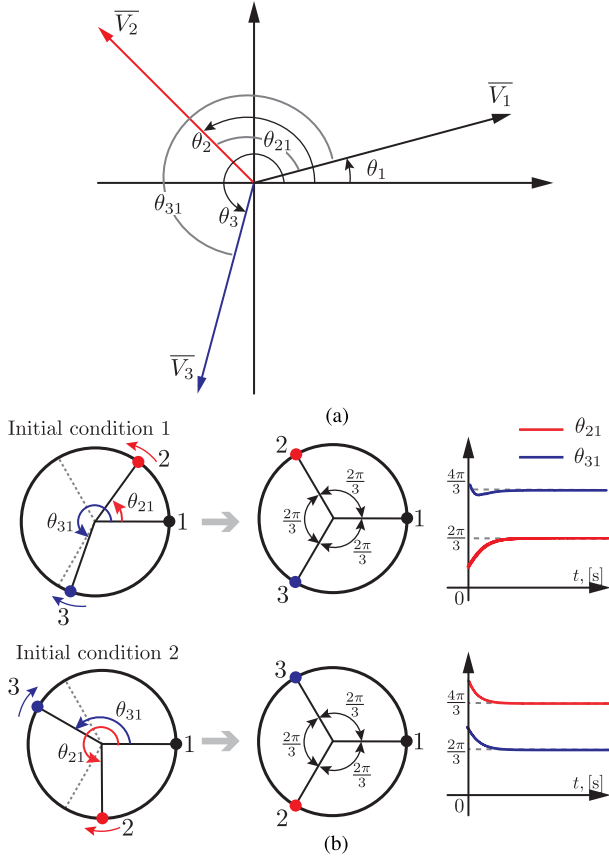


Fig. 5. (a) Polar diagram illustrating definitions of phase angles and relative differences. (b) Representative simulation results illustrate angle dynamics and establish that phase ordering in steady state depends on the initial conditions.

A. Phase Angle Difference Dynamics

We pick the angle of inverter #1 as the reference angle, and examine the evolution of angle differences with respect to θ_1 . To that end, we introduce $\theta_{21} = \theta_2 - \theta_1$ and $\theta_{31} = \theta_3 - \theta_1$. [See Fig. 5(a).] With the aid of (12b) and a combination of algebraic and trigonometric manipulations, we get the following dynamics for θ_{21} and θ_{31} :

$$\dot{\theta}_{21} = \dot{\theta}_2 - \dot{\theta}_1 \quad (13a)$$

$$= \frac{m_p V_2 V_1}{|\bar{Z}_{\text{loop}}|} \cos(\theta_{21} - \phi) + \frac{m_p V_3 V_1}{|\bar{Z}_{\text{loop}}|} \cos(\theta_{31} - \phi) - \frac{m_p V_2 V_3}{|\bar{Z}_{\text{loop}}|} \cos(\theta_{23} - \phi) - \frac{m_p V_2 V_1}{|\bar{Z}_{\text{loop}}|} \cos(\theta_{12} - \phi)$$

$$\begin{aligned} \dot{\theta}_{31} &= \dot{\theta}_3 - \dot{\theta}_1 \\ &= \frac{m_p V_3 V_1}{|\bar{Z}_{\text{loop}}|} \cos(\theta_{31} - \phi) + \frac{m_p V_2 V_1}{|\bar{Z}_{\text{loop}}|} \cos(\theta_{21} - \phi) \\ &\quad + \frac{m_p V_2 V_3}{|\bar{Z}_{\text{loop}}|} \cos(\theta_{23} - \phi) + \frac{m_p V_1 V_3}{|\bar{Z}_{\text{loop}}|} \cos(\theta_{13} - \phi). \end{aligned} \quad (13b)$$

Substituting for V_1 , V_2 , and V_3 from (12a) in the expressions above, ignoring terms that involve products of the form,

$m_p m_q^2$, $m_p m_q$, and defining

$$K = m_p \frac{V_{\text{nom}}^2}{|\bar{Z}_{\text{loop}}|} \quad (14)$$

we can approximate the dynamics of θ_{21} and θ_{31} as follows:

$$\begin{aligned} \dot{\theta}_{21} &\approx K(2 \sin \theta_{21} + \sin \theta_{31} + \sin(\theta_{21} - \theta_{31})) \sin \phi \\ &\quad + K(\cos \theta_{31} - \cos(\theta_{21} - \theta_{31})) \cos \phi \end{aligned} \quad (15a)$$

$$\begin{aligned} \dot{\theta}_{31} &\approx K(2 \sin \theta_{31} + \sin \theta_{21} + \sin(\theta_{31} - \theta_{21})) \sin \phi \\ &\quad + K(\cos \theta_{21} - \cos(\theta_{31} - \theta_{21})) \cos \phi. \end{aligned} \quad (15b)$$

See Appendix A for the detailed justifications on the approximations that lead to (15). Fig. 5(b) shows the trajectories of θ_{21} and θ_{31} generated by numerical simulation of (15a) and (15b) for two different initial conditions. (Subset of parameters utilized for the simulations are reported in Table I.) In both cases, we see the trajectories converging to a phase-balanced steady state. However, note that the phase orderings, 1 – 2 – 3 and 1 – 3 – 2, are both possible in steady state. Building on this simulation to guide analysis, we next uncover equilibria of (15a)–(15b) and characterize their small-signal stability.

B. Equilibria and Small-Signal Stability

Equilibria of dynamics in (15) are denoted by $\theta_{21,\text{eq}}$ and $\theta_{31,\text{eq}}$. These are values of θ_{21} and θ_{31} for which $\dot{\theta}_{21} = 0$ and $\dot{\theta}_{31} = 0$. The vector-field plots in Fig. 6 illustrate state trajectories for three different choices of impedance angle ϕ and, thereby facilitates our examination of system equilibria. (Parameters reported in Table I are utilized for the simulations.) From the figure, we can identify three types of equilibria: 1) stable (marked “●”), 2) unstable (marked “○”), and 3) saddle points (marked “⊙”). Notice that the two equilibria in $(\theta_{21,\text{eq}}, \theta_{31,\text{eq}})$ ● correspond to phase-balanced operation; the filled-in circle signifying attractive behavior in all directions. On the other hand, equilibria corresponding to $(\theta_{21,\text{eq}}, \theta_{31,\text{eq}})$ ⊙ are attractive in two directions and repulsive in the others. Finally, $(\theta_{21,\text{eq}}, \theta_{31,\text{eq}})$ ○ are repulsive in all directions [20].

Within one cycle, $[0, 2\pi)$, we can express the equilibria in the following form:

$$(\theta_{21,\text{eq}}, \theta_{31,\text{eq}})^\bullet = \left\{ \left(\frac{2\pi}{3}, \frac{4\pi}{3} \right), \left(\frac{4\pi}{3}, \frac{2\pi}{3} \right) \right\}$$

$$(\theta_{21,\text{eq}}, \theta_{31,\text{eq}})^\circ = \{(0, 0)\}$$

$$(\theta_{21,\text{eq}}, \theta_{31,\text{eq}})^\odot = \{(0, \sigma_1), (\sigma_1, 0), (\sigma_2, \sigma_2)\}$$

where for $\phi \in (0, \pi/2]$, σ_1, σ_2 are given by

$$\sigma_1 = 2\pi + 2 \tan^{-1}(-3 \tan \phi), \quad \sigma_2 = 2 \tan^{-1}(3 \tan \phi).$$

The plots in Fig. 6 provide an intuitive visualization for system dynamics and allow us to uncover all possible equilibria. For instance, the closed-form analytical characterization of σ_1 and σ_2 follow from searching for equilibria of (15) along $\theta_{21} = 0$, $\theta_{31} = 0$, and $\theta_{21} = \theta_{31}$, as hinted by the trajectories in Fig. 6.

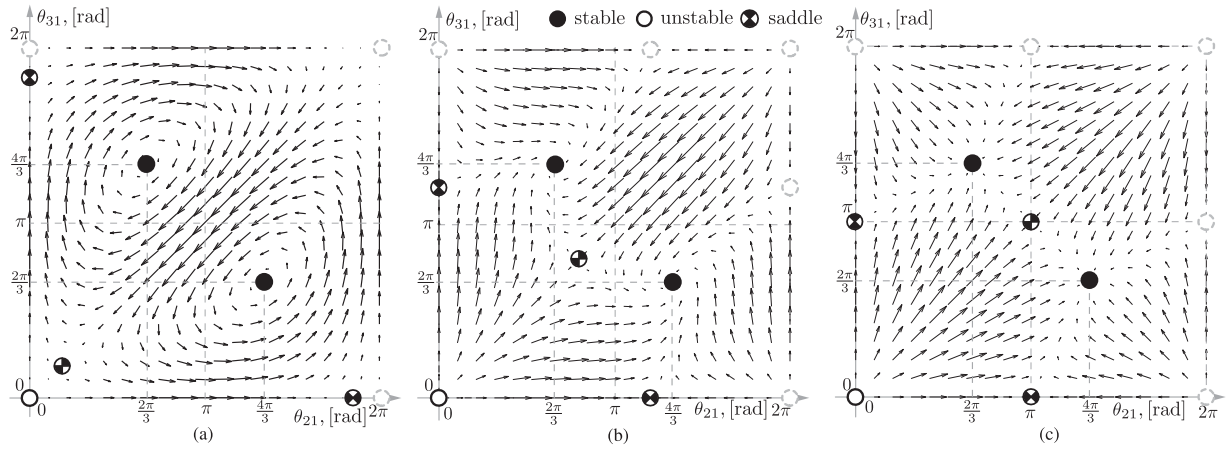


Fig. 6. Vector-fields for various delta-loop impedance angles. (a) $\phi = 0.1$ rad (mainly resistive). (b) $\phi = \frac{\pi}{4}$ rad (mixed RL). (c) $\phi = \frac{\pi}{2}$ rad (purely inductive). Stable equilibria are marked “●”, unstable equilibria are marked “○”, and saddle points are marked “⊗”.

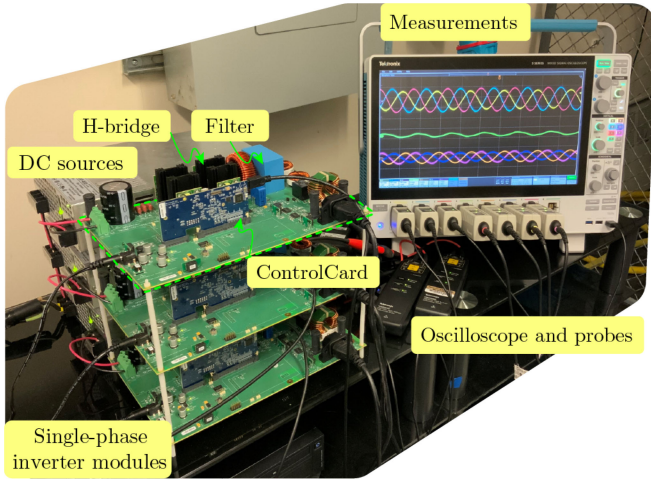


Fig. 7. Photograph of the experimental setup.

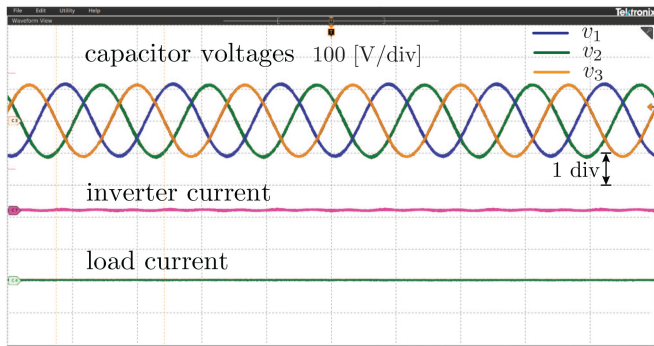


Fig. 8. Steady-state operation of delta-connected inverters with no load demonstrating phase-balanced operation.

Next, we demonstrate small-signal stability analytically. Express the dynamics of the small-signal model as

$$\begin{bmatrix} \Delta \dot{\theta}_{21} \\ \Delta \dot{\theta}_{31} \end{bmatrix} = \mathcal{J}(\theta_{21,eq}, \theta_{31,eq}) \begin{bmatrix} \Delta \theta_{21} \\ \Delta \theta_{31} \end{bmatrix}$$

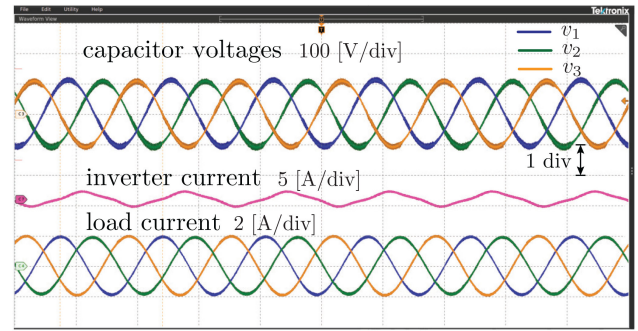
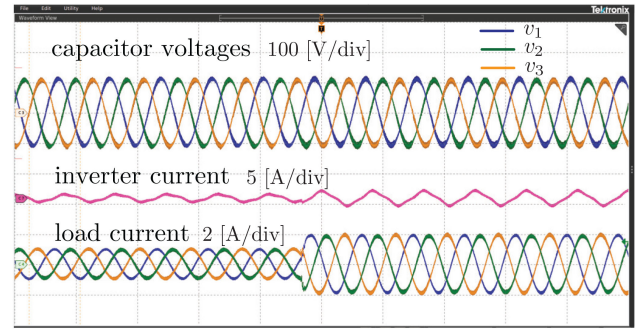
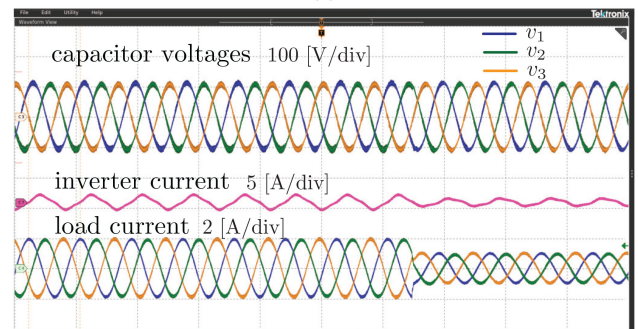


Fig. 9. Steady-state operation of delta-connected inverters with wye-connected resistive loads demonstrating phase-balanced operation.



(a)



(b)

Fig. 10. Transient performance during load steps. (a) loads step up. (b) loads step down.

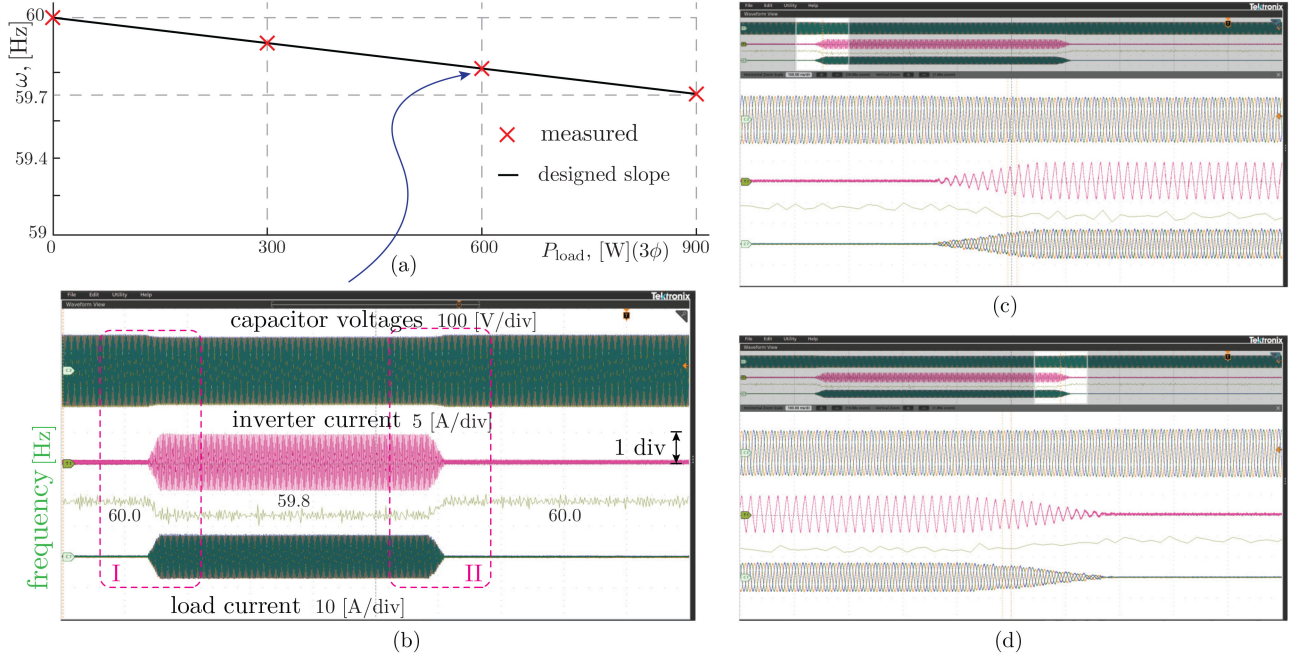


Fig. 11. Frequency regulation under various loads. (a) Measured and designed droop slopes. (b) Ramp load changes reflect frequency changes. (c) Inset I. (d) Inset II.

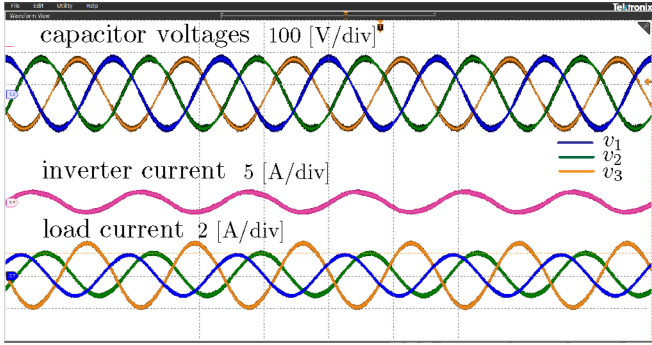


Fig. 12. Demonstrating phase-balanced operation with unbalanced loading.

where $\Delta\theta_{21}$ and $\Delta\theta_{31}$ denote small perturbations around the equilibria $\theta_{21,eq}$ and $\theta_{31,eq}$, and \mathcal{J} is the Jacobian matrix. The entries of the Jacobian matrix are specified in (11). Exponential stability of such a system is guaranteed if and only if all eigenvalues of \mathcal{J} have strictly negative real parts. Now we characterize the system eigenvalues for all equilibria for $\phi \in (0, \pi/2]$. Eigenvalues corresponding to the equilibria in $(\theta_{21,eq}, \theta_{31,eq})^\bullet$ are

$$\lambda_{1,2}^\bullet = -\frac{3}{2}K(\sin \phi \pm j \cos \phi). \quad (16)$$

Clearly, $\Re(\lambda_{1,2}^\bullet) < 0$, thereby establishing these equilibria to be small-signal stable. The equilibria in $(\theta_{21,eq}, \theta_{31,eq})^\circ$ have eigenvalues

$$\lambda_{1,2}^\circ = 3K \sin \phi. \quad (17)$$

Since $\Re(\lambda_{1,2}^\circ) > 0$, these equilibria are therefore, unstable. Finally, eigenvalues corresponding to all equilibria in

$(\theta_{21,eq}, \theta_{31,eq})^\bullet$ can be expressed as

$$\begin{aligned} \lambda_1^\bullet &= -3K \sin \phi, \\ \lambda_2^\bullet &= 9K \frac{1 + \tan^2 \phi}{1 + 9 \tan^2 \phi} \sin \phi. \end{aligned} \quad (18)$$

Given that $\Re(\lambda_1^\bullet) < 0$ and $\Re(\lambda_2^\bullet) > 0$, we see that these equilibria are saddle points.

V. EXPERIMENTAL VERIFICATION

In this section, we experimentally verify the phase-balanced operating condition in a hardware setup comprised of three delta-connected single-phase voltage source inverters. The hardware system is shown in Fig. 7. Each inverter is rated for 500 W, and is equipped with the *LCL* output-filter structure shown in Fig. 2. The physical-hardware and control-software parameters are listed in Table I. The controller is digitally implemented on a Texas Instruments TMS320F28379D controlCARD. Unless stated otherwise, all three inverters in the experiments below are set up identically with the same controllers, and they are issued the same nominal voltage magnitude and frequency values. Measured waveforms include the filter-capacitor voltages, grid-side currents, and load currents.

A. Steady-State and Transient Operations

We first consider an experiment with no load. As observed in Fig. 8, the three inverter voltages are balanced with $2\pi/3$ offsets, and they operate at nominal frequency and amplitudes. Results for the case when the inverter system is connected to wye-connected resistive loads are shown in Fig. 9. Again, we observe balanced operation in this setting as well. A close-up

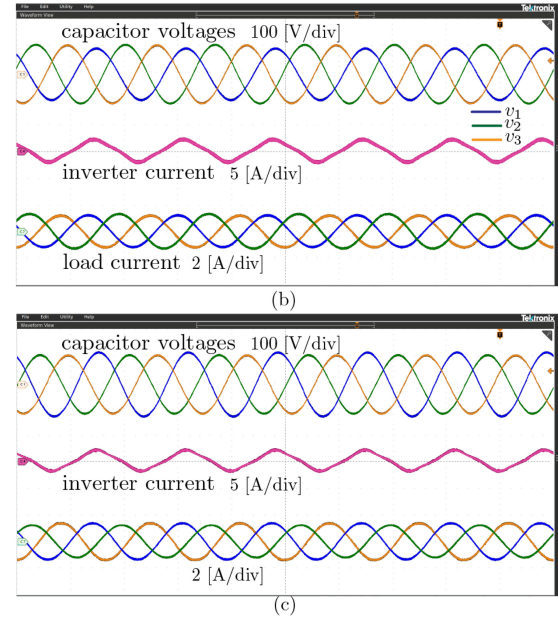
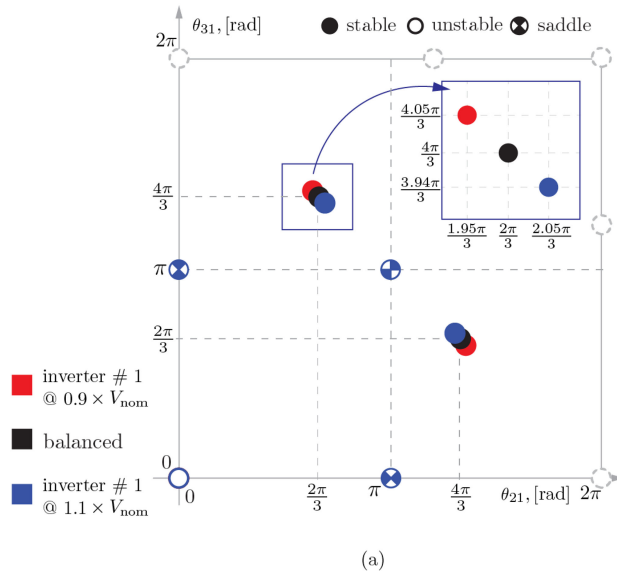


Fig. 13. Examining phase-balanced operation under unbalanced voltage commands. (a) Simulation results. and (b) and (c) Corresponding experiments for: nominal voltage of inverter #1 set to $0.9 \times V_{\text{nom}}$, with nominal voltages for inverters #2, 3 retained at V_{nom} ; and nominal voltage for inverter #1 set to $1.1 \times V_{\text{nom}}$, with nominal voltages for inverters #2, 3 retained at V_{nom} .

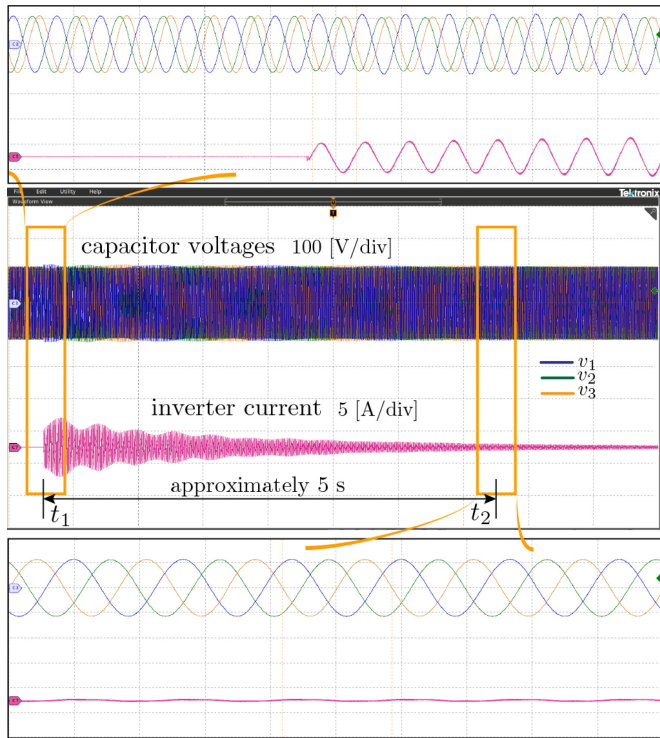


Fig. 14. View of dynamics during system's start up. Initial conditions are randomized, but the system converges to phase-balanced operation in steady state with no external communication.

inspection of the measured currents flowing within the inverter delta loop reveals the presence of a third-harmonic component. This harmonic originates from PWM nonlinearities in our particular implementation and our use of a modest dead time at the

zero-crossing transitions. We remark on this because although this effect might catch the eye of an observant reader, it has no observable impact on the effectiveness of our approach in obtaining phase-balanced operation. It is also interesting to note that the delta connection traps $3n$ th-order ($n = 1, 2, \dots$) harmonics within the loop such that load-waveform quality is maintained.

Transient performance is examined next. Waveforms during step changes between 300 and 600 W are shown in Fig. 10. These demonstrate tight voltage regulation and swift current adjustments during and after the step-up/down changes. Notice that phase-balanced operation is maintained through these large-signal changes. Measurements in Fig. 11 verify the intended power-frequency droop across the load range. In addition to the unit-level grid-forming capabilities offered by each inverter, we also show that the system of delta-connected units can self-organize into a three-phase system to provide power to loads.

B. Unbalanced Conditions

Practical systems are expected to encounter imbalances in both phase-voltage amplitudes and load demands. With regards to load imbalances, we refer to the circuit in Fig. 4(c) and note that load heterogeneity leads to imbalances in the currents $\bar{I}_{L\ell}$. However, \bar{I}_c is affected to a much lesser extent since it flows only within the delta loop. Since \bar{I}_c dominates angular dynamics, phase angle balancing is quite robust against load imbalances. The waveforms in Fig. 12 substantiate this statement and were taken for the setting where inverter #3 delivers twice as much power as the other two inverters.

Shifting focus to voltage amplitude imbalances, we consider an experiment where inverter #1 has an amplitude imbalance

such that $V_1 \neq V_2 = V_3$. To evaluate this condition, consider the vector field in Fig. 13(a) which shows the equilibria for two cases: 1) the nominal voltage of inverter #1 is set to be $0.9 \times V_{\text{nom}}$, while the nominal voltages for the inverters #2, 3 are retained at V_{nom} ; 2) the nominal voltage for inverter #1 is set to be $1.1 \times V_{\text{nom}}$, while the nominal voltages for the inverters #2, 3 are fixed at V_{nom} . An up-close inspection reveals that the voltage imbalance marginally impacts the stable angle equilibria. Hence, the system converges to angles that are very close to the balanced configuration irrespective of voltage imbalances. Measurements in Fig. 13(b) and (c) show corresponding experiments to substantiate this for the aforementioned voltage-magnitude imbalances. The conclusion to be drawn from the examination of these unbalanced conditions is that the system can continue to offer phase-balanced behavior in practical settings.

C. System Start-Up

Consider the setting where the system is energized from random initial conditions with an open-circuited delta loop. Results for this setting are illustrated in Fig. 14. A relay connected within the delta structure is used to close and open the delta loop, and a start-up resistor is added to avoid inrush currents within the delta loop when the inverters are initially connected. At time instant t_1 , the relay is closed to restore the delta connection. This enables the system to reach the phase-balanced condition after approximately 5 s till time instant t_2 . The start-up resistor is shorted out of the loop after steady state is reached and maintained.

VI. CONCLUSION

In this article, we investigated the possibility of using decentralized single-phase GFM inverters to form the foundation of balanced three-phase systems. Our analysis revealed that delta-connected inverters with droop control exhibit repulsive angular dynamics and are able to spontaneously reach phase balancing without any communication. We modeled and analyzed a system of three single-phase inverters in the phasor domain and derived relevant system dynamics. Small-signal stability analysis revealed that the stable system equilibria coincide with phase-balanced conditions where each phase is offset by $1/3$ of an ac cycle. Finally, experiments on a system of three delta-connected single-phase inverters substantiated the proposed framework and demonstrated robustness against voltage and load imbalances.

Future work will be focused on the derivation of system dynamics and investigating the feasibility of obtaining (innately or with additional control) phase-balanced operation with three-phase transformers, larger numbers of inverters in complex networks, and various wiring schemes, such as four-wire systems. In particular, we wish to establish a generic analytical framework to examine the setting where large numbers of low-voltage single-phase GFM units couple through the delta-wired sides of transformers across systems. A generalized treatment that exhaustively acknowledges heterogeneity in network parameters, control parameters, and loading across phases would also be a pertinent direction to explore.

APPENDIX

A. Details on Approximations Leading to (15)

The phase angle difference dynamics θ_{21} from (13a) can be rewritten as

$$\begin{aligned} \dot{\theta}_{21} &= \dot{\theta}_2 - \dot{\theta}_1 \\ &= \frac{m_p}{|\bar{Z}_{\text{loop}}|} ((2V_2V_1 \sin \theta_{21} + V_3V_1 \sin \theta_{31} + V_2V_3 \sin \theta_{23}) \sin \phi \\ &\quad + (V_3V_1 \cos \theta_{31} - V_3V_2 \cos \theta_{32}) \cos \phi). \end{aligned}$$

Taking the first term of the equation above as an example, we substitute the V_1 and V_2 expressions from (12a) and obtain

$$\begin{aligned} \frac{m_p V_2 V_1}{|\bar{Z}_{\text{loop}}|} &= \frac{m_p V_{\text{nom}}^2}{|\bar{Z}_{\text{loop}}|} + \frac{m_p m_q V_{\text{nom}}}{|\bar{Z}_{\text{loop}}|^2} \\ &\quad \left(\sum_{k=1}^3 V_k V_2 \sin(\theta_{k2} - \phi) + \sum_{j=1}^3 V_j V_1 \sin(\theta_{j1} - \phi) \right) \\ &\quad + \frac{m_p m_q^2}{|\bar{Z}_{\text{loop}}|^3} \left(\sum_{k=1}^3 V_k V_2 \sin(\theta_{k2} - \phi) \sum_{j=1}^3 V_j V_1 \sin(\theta_{j1} - \phi) \right). \end{aligned}$$

Ignoring higher order terms, that involve products of the form $m_p m_q^2, m_p m_q$, we obtain

$$\begin{aligned} \dot{\theta}_{21} &= \dot{\theta}_2 - \dot{\theta}_1 \approx \frac{m_p V_{\text{nom}}^2}{|\bar{Z}_{\text{loop}}|} ((2 \sin \theta_{21} + \sin \theta_{31} + \sin \theta_{23}) \sin \phi \\ &\quad + (\cos \theta_{31} - \cos \theta_{32}) \cos \phi) \end{aligned}$$

which maps to (15a) with the definition for K in (14). Dynamics of $\dot{\theta}_{31}$ follow similarly.

REFERENCES

- [1] X. Wang, "Resurgence of grid-forming inverter technology," *IEEE Electr. Mag.*, vol. 10, no. 1, pp. 5–6, Mar. 2022.
- [2] B. Johnson et al., "A generic primary-control model for grid-forming inverters: Towards interoperable operation & control," in *Proc. Hawaii Int. Conf. Syst. Sci.*, 2022, pp. 3398–3407.
- [3] A. Hintz, U. Prasanna, and K. Rajashekara, "Comparative study of the three-phase grid-connected inverter sharing unbalanced three-phase and/or single-phase systems," *IEEE Trans. Ind. Appl.*, vol. 52, no. 6, pp. 5156–5164, Nov./Dec. 2016.
- [4] Y. Karimi, H. Oraee, and J. M. Guerrero, "Decentralized method for load sharing and power management in a hybrid single/three-phase-islanded microgrid consisting of hybrid source PV/Battery units," *IEEE Trans. Power Electron.*, vol. 32, no. 8, pp. 6135–6144, Aug. 2017.
- [5] J. Simpson-Porco, F. Dörfler, and F. Bullo, "Droop-controlled inverters are Kuramoto oscillators," *IFAC Proc. Volumes*, vol. 45, no. 26, pp. 264–269, 2012.
- [6] M. Sinha, F. Dörfler, B. Johnson, and S. Dhople, "Uncovering droop control laws embedded within the nonlinear dynamics of Van der Pol oscillators," *IEEE Control Netw. Syst.*, vol. 4, no. 2, pp. 347–358, Feb. 2017.
- [7] O. Ajala, N. Baeckeland, S. Dhople, and A. Domínguez-García, "Uncovering the Kuramoto model from full-order models of grid-forming inverter-based power networks," in *Proc. IEEE Conf. Decis. Control*, 2021, pp. 4944–4949.
- [8] R. Sepulchre, D. A. Paley, and N. E. Leonard, "Stabilization of planar collective motion: All-to-all communication," *IEEE Trans. Autom. Control*, vol. 52, no. 5, pp. 811–824, May 2007.
- [9] D. A. Paley, N. E. Leonard, and R. Sepulchre, "Oscillator models and collective motion: Splay state stabilization of self-propelled particles," in *Proc. 44th IEEE Conf. Decis. Control*, 2005, pp. 3935–3940.

- [10] M. Sinha, F. Dörfler, B. Johnson, and S. Dhople, "Phase balancing in globally connected networks of Liénard oscillators," in *Proc. IEEE 56th Annu. Conf. Decis. Control*, 2017, pp. 595–600.
- [11] M. Sinha, J. Poon, B. Johnson, M. Rodriguez, and S. Dhople, "Decentralized interleaving of parallel-connected buck converters," *IEEE Trans. Power Electron.*, vol. 34, no. 5, pp. 4993–5006, May 2019.
- [12] M. Sinha, S. Dhople, B. Johnson, M. Rodriguez, and J. Poon, "Decentralized interleaving of paralleled DC-DC buck converters," in *Proc. IEEE 18th Workshop Control Model. Power Electron.*, 2017, pp. 1–6.
- [13] J. Poon, B. Johnson, S. V. Dhople, and J. Rivas-Davila, "Decentralized carrier phase shifting for optimal harmonic minimization in asymmetric parallel-connected inverters," *IEEE Trans. Power Electron.*, vol. 36, no. 5, pp. 5915–5925, May 2021.
- [14] S. Dutta et al., "Decentralized carrier interleaving in cascaded multilevel DC-AC converters," in *Proc. IEEE 20th Workshop Control Model. Power Electron.*, 2019, pp. 1–6.
- [15] M. Sinha, F. Dörfler, B. Johnson, and S. Dhople, "Stabilizing phase-balanced or phase-synchronized trajectories of Van der Pol oscillators in uniform electrical networks," in *Proc. 56th Annu. Allerton Conf. Commun. Control Comput.*, 2018, pp. 335–340.
- [16] M. C. Chandorkar, D. M. Divan, and R. Adapa, "Control of parallel connected inverters in standalone AC supply systems," *IEEE Trans. Ind. Appl.*, vol. 29, no. 1, pp. 136–143, Jan. 1993.
- [17] D. Pan, X. Wang, F. Liu, and R. Shi, "Transient stability of voltage-source converters with grid-forming control: A design-oriented study," *IEEE Trans. Emerg. Sel. Topics Power Electron.*, vol. 8, no. 2, pp. 1019–1033, Jun. 2020.
- [18] A. E. Kennelly, "The equivalence of triangles and three-pointed stars in conducting networks," *Elect. World Engineer*, vol. 34, no. 12, pp. 413–414, 1899.
- [19] J. Bird, *Electrical Circuit Theory and Technology*. New York, NY, USA: Oxford, 2001.
- [20] H. Khalil, *Nonlinear Systems*, 3rd ed. Englewood Cliffs, NJ, USA: Prentice Hall, 2002.